

# Modulation of the optical and transport properties of epitaxial SrNbO<sub>3</sub> thin films by defect engineering

Cite as: J. Appl. Phys. 135, 015303 (2024); doi: 10.1063/5.0179267

Submitted: 30 September 2023 · Accepted: 13 December 2023 ·

Published Online: 5 January 2024



Shammi Kumar,<sup>1,a)</sup> Jibril Ahammad,<sup>2</sup> Dip Das,<sup>1,b)</sup> Rakesh Kumar,<sup>1</sup> Sankar Dhar,<sup>1</sup> and Priya Johari<sup>1,a)</sup>

## AFFILIATIONS

<sup>1</sup>Department of Physics, School of Natural Sciences, Shiv Nadar Institution of Eminence (Deemed to be University), Gautam Buddha Nagar, Uttar Pradesh 201314, India

<sup>2</sup>Department of Physics, Auburn University, Auburn, Alabama 36830, USA

**Note:** This paper is part of the Special Topic on: Native Defects, Impurities and the Electronic Structure of Compound Semiconductors: A Tribute to Dr. Wladyslaw Walukiewicz.

<sup>a)</sup>Authors to whom correspondence should be addressed: sk657@snu.edu.in and priya.johari@snu.edu.in

<sup>b)</sup>Present address: Department of Electronic and Electrical Engineering, University College London, Torrington Place, London WC1E7JE, United Kingdom.

## ABSTRACT

The discovery of strontium niobate (SNO) as a potentially new transparent electrode has generated much interest due to its implications in various optoelectronic devices. Pristine SNO exhibits exceptionally low resistivity ( $\sim 10^{-4} \Omega \text{ cm}$ ) at room temperature. However, this low resistivity occurs due to large number of carrier concentration in the system, which significantly affects its optical transparency ( $\sim 40\%$ ) in the visible range and hinders its practical applications as a transparent electrode. Here, we show that modulating the growth kinetics via oxygen manipulation is a feasible approach to achieve the desired optoelectronic properties. In particular, epitaxial (001) SNO thin films are grown on (001) lanthanum aluminate by pulsed laser deposition at different oxygen partial pressures and are shown to improve the optical transparency from 40% to 72% ( $\lambda = 550 \text{ nm}$ ) at a marginal cost of electrical resistivity from 2.8 to  $8.1 \times 10^{-4} \Omega \text{ cm}$ . These changes are directly linked with the multi-valence Nb-states, as evidenced by x-ray photoelectron spectroscopy. Furthermore, the defect-engineered SNO films exhibit multiple electronic phases that include pure metallic, coexisting metal-semiconducting-like, and pure semiconducting-like phases as evidenced by low-temperature electrical transport measurements. The intriguing metal-semiconducting coexisting phase is thoroughly analyzed using both perpendicular and angle-dependent magnetoresistance measurements, further supported by a density functional theory-based first-principles study and the observed feature is explained by the quantum correction to the conductivity. Overall, this study shows an exciting avenue for altering the optical and transport properties of SNO epitaxial thin films for their practical use as a next-generation transparent electrode.

Published under an exclusive license by AIP Publishing. <https://doi.org/10.1063/5.0179267>

## I. INTRODUCTION

Transition metal oxides (TMOs) occupy a central role in the worldwide demand for electronic devices. They exhibit a wide range of functionality owing to their tunability to suit different kinds of applications. Among a plethora of TMOs that are explored,<sup>1–7</sup> strontium niobate (SNO) has gained much attention

due to its practical applications such as strong photocatalytic activity,<sup>1</sup> large magnetoresistance,<sup>8,9</sup> and ferroelectricity.<sup>10</sup> It is also used to fabricate new generation plasmonic devices<sup>11–15</sup> and prepare transparent electrodes.<sup>3,11,12,16,17</sup> SNO in its bulk form is a wide band gap insulator ( $E_g \sim 4.1 \text{ eV}$ ) having an orthorhombic structure ( $a = 4.05 \text{ \AA}$ ,  $b = 27.72 \text{ \AA}$ ,  $c = 5.78 \text{ \AA}$ ) with a chemical composition of SrNbO<sub>3.5</sub>. However, epitaxial thin films of SNO, mostly grown by

pulsed laser deposition (PLD),<sup>11,13,15,16,18,19</sup> typically synthesize in a tetragonal phase with a composition of  $\text{SrNbO}_3$  on various closely matched substrates. These thin films reportedly show good electronic properties due to a large number of free electron carrier concentrations arising mainly from oxygen vacancies and charge state of Nb, via manipulation of ambient oxygen partial pressure ( $p\text{O}_2$ ) and deposition temperature during the growth process. For example, Wan *et al.*<sup>16</sup> as well as Oka *et al.*<sup>20</sup> reported the resistivities of such PLD grown epitaxial thin films ranging from 10 to  $28\ \mu\Omega\text{ cm}$  and mobility from  $2.47\text{--}16\text{ cm}^2\text{ V}^{-1}\text{ s}^{-1}$  depending on the residual strain that arises from the substrate,  $p\text{O}_2$ , the background vacuum, and deposition temperature during the thin film growth process. Through XPS, Bigi *et al.*<sup>21</sup> have also shown independently that Nb is in a 4+ state, which is responsible for the metallic state in these thin films. It may be noted that Nb has a 5+ state in bulk SNO, which is responsible for its insulating properties, due to non-availability of 4d free electrons.<sup>22</sup> Further, Wan *et al.*<sup>16</sup> also demonstrate that the homogeneous chemical composition of the  $\sim 100\text{ nm}$  SNO thin films is  $\text{SrNbO}_x$  by O-resonant Rutherford backscattering spectroscopy (RBS). For metallic films (grown under  $p\text{O}_2 = 10^{-6}\text{ mbar}$ ),  $x$  is found to be  $\sim 3$ , while for insulating films (grown under  $p\text{O}_2 = 10^{-4}\text{ mbar}$ )  $x$  is found to be  $\sim 3.5$ . Due to the pristine growth condition in background vacuum ( $10^{-7}\text{--}10^{-8}\text{ mbar}$ ), no other elemental impurities are observed. The theoretical calculations performed in the same report for different O stoichiometry also demonstrate a metal to insulator transition when  $x$  changes from 3 to 3.5.

Another interesting property of  $\text{SrNbO}_3$  is its high bandgap ( $\sim 4.1\text{--}4.9\text{ eV}$ ),<sup>11,23</sup> which makes it ideal to use it in transparent conducting oxides (TCOs). However, due to the high amount of free carrier concentration ( $\sim 10^{22}\text{ cm}^{-3}$ ), a significant contribution of free carrier absorption (FCA) is encountered in the visible region, which makes it highly absorbing in the visible region. So, to make a SNO as a visible transparent electrode, it is necessary to reduce the FCA. One way to do this is by reducing the carrier concentration to significantly minimize the FCA, which increases the transparency. This can be done by changing the stoichiometry of O in SNO, which increases the oxidation state of Nb from 4+ to 5+ and decreases the amount of free electron in the system. This approach has been applied theoretically by Khan *et al.*<sup>24</sup> and experimentally by Asmara *et al.*<sup>25</sup> where the reduction in carrier concentration is shown to have an increase in the transparency by the modulation of O content in SNO. However, as Wan *et al.*<sup>16</sup> and Di Pietro *et al.*<sup>26</sup> have observed that such an increase in the O content increases the resistivity drastically, and thus hinders its potential in TCOs. Previous studies on such a metal-insulator or metal-semiconductor transition have either been studied as a function of thickness,<sup>27,28</sup> growth temperature,<sup>29</sup> or as a function of doping<sup>30,31</sup> in TMOs. However, the mechanism behind such a transition due to the influence of O is poorly understood and needs to be considered carefully for successfully designing the next-generation devices. Thus, it becomes mandatory to understand the effect of O manipulation on the electronic properties and understand the cause of the underlying mechanism behind such a transition experimentally.

In the present study, we therefore study and report the interdependence of structural, electronic, and magnetic properties of

epitaxial (001) SNO thin films, grown on (001)  $\text{LaAlO}_3$  (LAO) using PLD under different  $p\text{O}_2$  ranging from  $10^{-6}$  to  $5 \times 10^{-5}\text{ mbar}$  to understand the influence of structural changes, viz., oxygen concentration on the structural, chemical, optical, electronic properties of strontium niobate. The growth pressure during thin film deposition determines the stoichiometry of strontium niobate and the composition of O in SNO can change from  $\sim 3$  to 3.5. This, in effect, changes the nature of the resistivity curves which have different behavior at low temperatures. This phenomenon is generally seen in strongly correlated oxides such as  $\text{SrVO}_3$ <sup>32</sup> and  $\text{SrMoO}_3$ <sup>28</sup> and the underlying mechanism has been explained by the quantum correction to the conductivity (QCC). The QCC, in turn, has contribution from two components, weak localization (WL) or renormalized electron-electron interaction (REEI). The dominance of REEI and WL within QCC can be distinguished using the magnetoresistance (MR) measurement, which shows a significant change with  $p\text{O}_2$ . Furthermore, due to the residual strain present in these films, angle-dependent magnetoresistance measurement is carried out and is shown to reveal interesting properties. To corroborate the metal-insulator transition of SNO, first-principles based density functional theory is performed on different stoichiometries of SNO, namely,  $\text{SrNbO}_3$  and  $\text{SrNbO}_{3.5}$ . The electronic behavior of  $\text{SrNbO}_3$  and  $\text{SrNbO}_{3.5}$  is then understood by the combined studies of the density of states and Bader charge analysis. The above studies prove the versatility of strontium niobate as a fantastic material, which can be modulated easily by different growth conditions, to be suitable for different applications of choice.

## II. METHODS

### A. Experimental details

Single phase  $\text{Sr}_2\text{Nb}_2\text{O}_7$  powder is synthesized by the solid-state reactions of  $\text{SrCO}_3$  (Alfa Aesar, 99.99%) and  $\text{Nb}_2\text{O}_5$  (Alfa Aesar, 99.9985%) powder after making their mixture in a proper molar ratio (2:1). They are hand ground using a mortar and pestle for 1 h and calcined at  $1100^\circ\text{C}$  for 48 h with intermediary grinding in every 24 h. The desired purity of the powder is confirmed by x-ray diffraction, after which the powder is compressed to a pellet of 1 in. in diameter using a hydraulic press. The pellet is then sintered for 24 h at  $1350^\circ\text{C}$  and used as a target material. The  $\text{SrNbO}_3$  thin films are deposited on  $\text{LaAlO}_3$  (001) substrates (MTI, USA) via PLD (Neocera, USA) using a Coherent Excimer KrF ultraviolet laser (Coherent GmbH, Germany) of the wavelength of 248 nm with a laser energy density of  $1.2\text{ J/cm}^2$ . The LAO substrates are first cleaned with isopropyl alcohol, then de-ionized water, and finally with acetone, before loading into the PLD chamber. For each sample, the deposition process starts when the base vacuum pressure reaches  $\sim 2 \times 10^{-7}\text{ mbar}$ , through a turbo molecular pump along with a dry backing pump (make-Pfeiffer, Germany) to eliminate the possible presence of any residual contaminants, such as organics, water vapor, hydroxides, etc. To start deposition, the oxygen partial pressure is set by a mass flow controller. The three films studied in this manuscript are deposited for 20 min at three partial pressures of  $\text{O}_2$ , namely,  $1 \times 10^{-6}$ ,  $10^{-5}$ , and  $5 \times 10^{-5}\text{ mbar}$  by providing a gas flow of 0, 0.65, and 1.5 SCCM, respectively (henceforth samples S1, S2, and S3). The distance of the target to substrate is kept fixed at 6 cm for all cases. The samples are thus

heated to 750 °C and a laser repetition rate of 2 Hz to enable best crystalline quality thin films. The samples are thus cooled down to room temperatures under the same  $p\text{O}_2$  flow before taking it out of the vacuum chamber.

The structural properties of the thin films as a function of  $p\text{O}_2$  are studied by high-resolution x-ray diffraction (HR-XRD) (D8-Advance, Bruker, Germany). The surface morphology is studied by atomic force microscopy (AFM) (Park XE-7, South Korea). The elemental analysis is performed with the help of a field emission scanning electron microscope (FESEM) (JEOL JSM 7600 Plus). The thickness of the thin films is determined *ex situ* using variable angle spectroscopic ellipsometry (VASE) (M-2000-UI, J. A. Woollam, USA) and Rutherford backscattering (RBS). High-resolution x-ray photoemission spectroscopy (HR-XPS) verifies constituents, the changes to the charge states of the thin films, and the binding energies of the samples. The XPS studies are performed using a PHI 5000 Versa probe III XPS system equipped with monochromatic Al-K $\alpha$  radiation. The XPS data are analyzed using CasaXPS software. Electronic and magnetic properties are studied using a physical property measurement system (PPMS) (Quantum Design, USA).

## B. Computational details

DFT based simulations are carried out on two structures of strontium niobate, namely,  $\text{SrNbO}_{3.5}$  with  $\text{Cmc}2_1$  space group, and  $\text{SrNbO}_3$  with  $\text{Pm}\bar{3}\text{m}$  space group using the Vienna *ab initio* simulation package (VASP)<sup>33</sup> to determine the atomic and electronic structures of SNO. The projector-augmented-wavefunction (PAW)<sup>33,34</sup> approach along with Perdew–Burke–Ernzerhof (PBE)<sup>35</sup> exchange correlation and an effective Hubbard potential, for the DFT + U approach as suggested by Dudarev *et al.*<sup>36</sup> is applied to treat the Nb 4*d* orbitals occupied by the  $\text{Nb}^{4+}$  ions present for SNO, the value of which is set at 4 eV. The orbitals chosen for the valence states of Sr, Nb, and O are 4*s*4*p*5*s*, 4*p*5*s*4*d*, and O2*s*2*p*, respectively. The cut-off energy for the plane-wave basis set is fixed to 1.5 times the maximum energy cut-off for O, i.e., 600 eV. The reciprocal space is sampled on a Gamma-centered mesh with a *k*-point resolution of 0.02 Å. For the electronic self-consistent calculations, the convergence criterion is set to be  $10^{-6}$  eV. The structural relaxation is done on both atomic and lattice positions till the Hellman–Feynman forces on each atom are less than  $10^{-2}$  eV/Å.

## III. RESULTS

### A. Structural properties

The thickness of the samples obtained through VASE is found to be 84, 75, and 70 nm for S1, S2, and S3, respectively [Figs. SI-1(a) and 1(b) in the [supplementary material](#)] giving an effective deposition rate of 4.2, 3.75, and 3.5 nm/min for  $10^{-6}$ ,  $10^{-5}$ , and  $5 \times 10^{-5}$  mbar, respectively. The thickness of the thin films is also confirmed independently by RBS (Fig. SI-2 in the [supplementary material](#)). These film deposition rates (340–300 monolayer/minute) on the substrates are much higher than the formation of oxygen layer, which varies in the range of 6–12 monolayers per minute.

The HR-XRD patterns of all these three thin films, namely, S1, S2, and S3 deposited in different oxygen partial pressures for a

constant growth temperature of 750 °C on a pseudocubic LAO (001) substrate are shown in Fig. 1(a). In all these cases, only the (001) family of peaks originating from both film and substrate are observed. For clarity, only the (002) SNO film peak along with the (002) LAO substrate peak is shown for each pattern since these (002) peaks have the highest intensities. As only the (001) family of peaks are observed, it can be inferred that the films are oriented along the (001) direction of the substrate. Moreover, it is clearly seen from these patterns that with increasing  $p\text{O}_2$ , the (002) SNO peaks is shifting toward higher  $2\theta$  angles indicating the contraction of out-of-plane lattice parameter (*c*). The experimental *c* values are  $\sim 4.1$ , 4.08, and 4.07 Å for S1, S2, and S3, respectively. Wan *et al.*<sup>16</sup> also found the same *c* of 4.1 Å for sample conditions of S1. It may be noted that the lattice parameter of LAO is 3.79 Å.

The in-plane XRD are also performed in all these samples, and almost similar patterns are observed in all the cases. A representative spectrum (sample S1) is shown in the inset of Fig. 1(a). The in-plane lattice parameters are found to be same in all cases and the value is  $a = 4.02$  Å. As there is a large lattice mismatch between the substrate ( $a = 3.79$  Å) and the film, it is expected that the in-plane lattice parameter of the film should be close to 3.79 Å, due to compressive strain. But the same in-plane lattice parameter of 4.02 Å implies that all the films are already relaxed at the thickness of  $\sim 70$  nm. A similar behavior for SNO films on LAO is obtained by Wan *et al.*,<sup>16</sup> in which the in-plane lattice parameter for all their samples deposited in the same pressure range used in the present study is found to be  $\sim 4.04$  Å, which is very close to the present experimental value.

Figure 1(b) shows the  $\phi$  scan of an asymmetric plane (103) for all the samples. It is clearly seen from the figure that all the films have a fourfold symmetry along the in-plane direction, indicating a cubic structure in the in-plane direction. Together, with all these results and the difference in *a* and *c* lattice parameters demonstrate that all the films are distorted cubic or tetragonal structures in nature.

The surface morphology of these films is studied with the help of FESEM. For representative purpose only, the results obtained from the sample S1 is shown in Fig. 2 as the results are similar in other two samples. Figure 2(a) shows the FESEM image of the SNO thin film deposited on the LAO substrate. Figure 2(a) shows the absence of any grain boundaries, droplet, or any spurious phases that might get introduced during the PLD growth process.<sup>37,38</sup> From the elemental mapping data of Nb, Sr, and O, combined with energy dispersive x-ray analysis (EDX) data (Fig. SI-3 in the [supplementary material](#)), it is clear that Sr and Nb have the same stoichiometric ratio of 1:1. Since the underlying substrate is LAO, the O contribution in the EDX data comes from both the thin film and the substrate. As a result of this, the exact determination of O in the film remains challenging. However, as films are distorted cubic or tetragonal in nature (as confirmed by XRD analysis), the composition of this film should be then  $\text{SrNbO}_{3\pm\delta}$ , which is also independently confirmed by RBS analysis. A typical RBS spectrum along with a fitted one is shown in Fig. SI-3 in the [supplementary material](#). As mentioned earlier, the other stable phase of SNO is orthorhombic in nature<sup>16</sup> whose composition is  $\text{SrNbO}_{3.5}$  and this phase is normally formed around

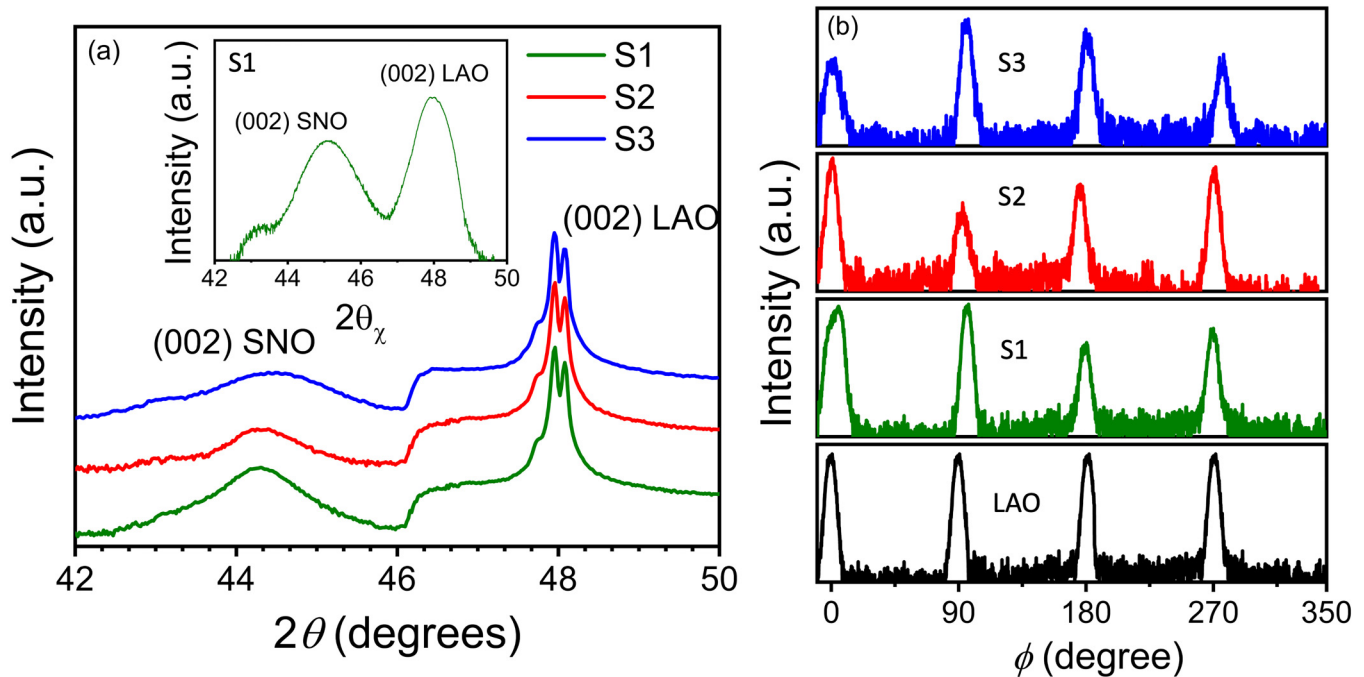


**FIG. 1.** (a) HR-XRD spectra of out-of-plane SNO (002) on LAO (001) substrates. Inset shows the in-plane XRD spectrum for (002) peak of SNO of sample S1 (b)  $\phi$ -scan of (103) planes of SNO shows four peaks separated by  $90^\circ$  that is indicative of tetragonal symmetry along the out-of-plane direction. It confirms the perovskite type tetragonal phase nature of the film. The black  $\phi$  scan peaks in (b) correspond to the LAO (001) substrate.

$1 \times 10^{-4}$  mbar, which is much higher than  $pO_2$  used in the present study. The surface morphology is further studied by AFM and is shown in Fig. 2(b). The surface of each sample scanned over the randomly selected areas is featureless and quite uniform with no

visible grains, pits, or deformities. The typical root mean square roughness for the surface for each film is found to be  $\sim 0.2$  nm, which is very good considering the underlying surface on which the film has grown has an average roughness of 0.4 nm.

06 January 2024 07:46:46

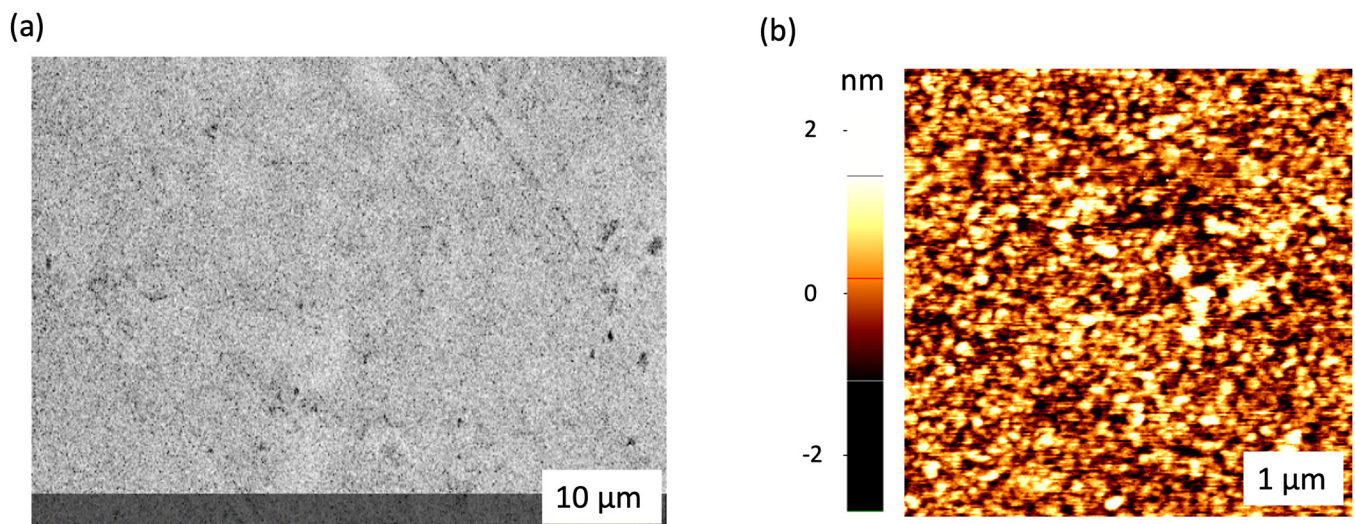


**FIG. 2.** (a) FESEM image and (b) AFM image of SNO thin films confirming the absence of any spurious phase, grain boundary, pits, or deformities.



## B. Chemical properties

To understand the influence of  $pO_2$  on the binding energy and elemental charge state of SNO, x-ray photoelectron spectroscopy (XPS) is carried out for samples S1 and S2 and is displayed in Fig. 3. The instrument is pre-calibrated using an Au-sputtered film as the reference sample, as it does not oxidize easily. The energy calibration is done by determining the  $4f_{7/2}$  peak position and comparing with the standard value of 83.96 eV. For determining the accurate binding energy, the experimental data obtained from these samples are calibrated by using the C 1s peak of C-C/C-H complex at 289.58 eV, as prescribed by Greczynski *et al.*<sup>39,40</sup> where the work function ( $\phi$ ) of SNO is considered to be 2.0 eV.<sup>41</sup>

The recorded Nb-3d spectra for S1 and S2 are carefully analyzed, and the deconvoluted peaks are presented in Figs. 3(c) and 3(d), respectively. Two spin-split peaks at  $\sim 290.7$  and 207 correspond to the  $3d_{5/2}$  and  $3d_{3/2}$  states of Nb<sup>4+</sup> at in its formal chemical state of +5. The deconvolution of those two peaks is done by considering a constant full width half maximum (FWHM), and the area is kept constant at 3:2. On the lower binding energy side (around 205 eV), the  $3d_{5/2}$  state is asymmetric, indicating the need for incorporating at least another chemical state of Nb in the fitting model.<sup>42,43</sup> The fitting method reveals two additional components at  $\sim 205.9$  and 208.5 eV [inset of Figs. 3(a) and 3(b)], corresponding to the  $3d_{5/2}$  and  $3d_{3/2}$  states with a +4 charge.<sup>42,43</sup> The complete details about the fitting are given in Table I. This contribution of Nb<sup>4+</sup> in S1 is comparable to the PLD grown highly metallic SNO thin films obtained by Bigi *et al.*<sup>21</sup> The change in the contribution of Nb<sup>4+</sup> implies a change in the number of free carriers in the system, as it is known that Nb changes its valency from 5+ to 4+ by donating a free electron to the system. The cumulative contribution of the +4 charge state is 10.5% for S1 and it decreases to

2.9% for S2. This change in the free electron concentration has a significant effect on the optical and electronic transport properties, which are discussed in Sec. III C.

## C. Optical and electronic properties

The optical transmission spectra of the SNO films formed on LAO at different  $pO_2$  are displayed in Fig. 4(a). In the visible range at 550 nm, the sample S1 had an average transparency of about 40%. Additionally, the sample exhibits a significant infrared absorption, which suggests a strong metallic nature. As the growth  $pO_2$  is increased, transparency also increases that gives a maximum transparency of  $\sim 72\%$  for sample S3. In spite of this large change in the transparency, the bandgap of the material remains same at  $\sim 4$  eV for all the three samples (see Fig. SI-4 in the [supplementary material](#) for absorbance data and Tauc's plot for the indirect bandgap). The increase in the transparency due to varying O composition in SNO can be understood from the term plasmon frequency. From the simplistic Drude model, the transparency of any material is dependent on the term plasmon frequency ( $\omega_p$ ) which is related to the carrier concentration as  $\omega_p \sim \sqrt{n/m^*}$ <sup>17</sup> ( $n$ : carrier concentration,  $m^*$ : effective mass). Any light which has angular frequency greater than  $\omega_p$  of the material is transparent whereas any light with a smaller energy than  $\omega_p$  is reflected back or absorbed and thus does not pass through the material. The measured  $\omega_p$  for SrNbO<sub>3</sub> is  $\sim 1.9$ – $2.0$  eV, which lies within the frequency range of visible light (1.75–3.10 eV). By modulating the content of O within SNO, and decreasing the overall carrier concentration within the system, Asmara *et al.*<sup>25</sup> have shown that  $\omega_p$  shifts to the lower edge of the visible spectrum as the growth  $pO_2$  is increased.  $\omega_p$  in Ref. 25 is found to vary from 1.9 to 1.7 eV as  $pO_2$  is changed from

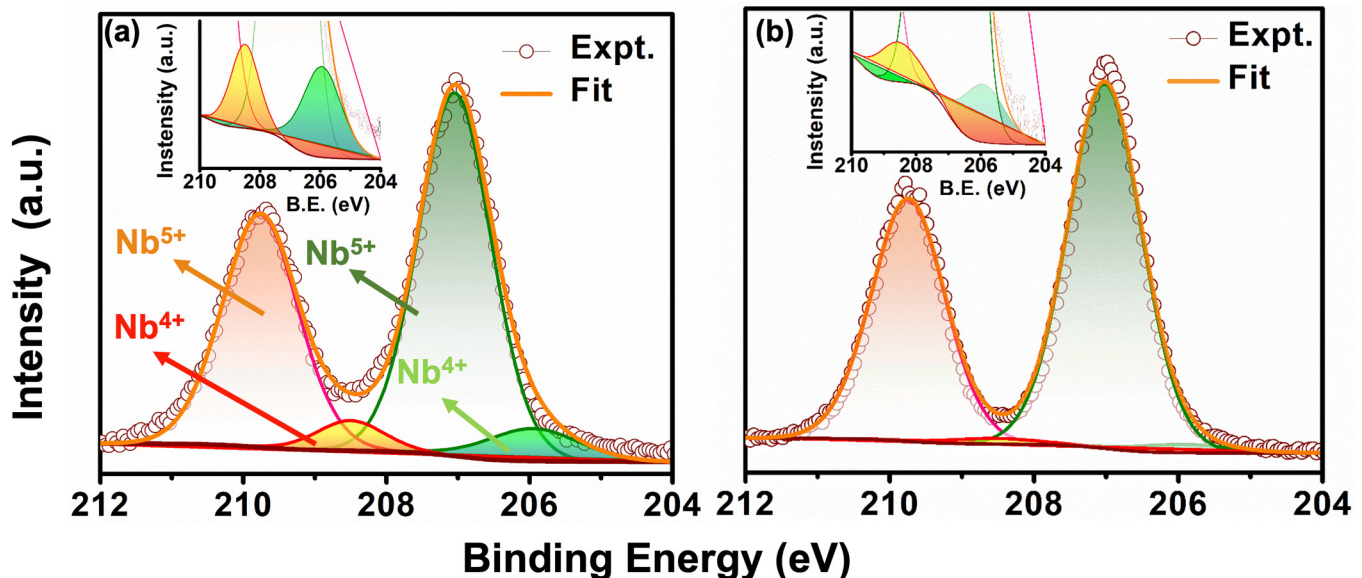


FIG. 3. Core-level x-ray photoemission spectra for Nb 3d thin films of SNO for (a) S1 and (b) S2. Inset in each figure shows the contribution of Nb<sup>4+</sup> in each case.

06 January 2024 07:46:46

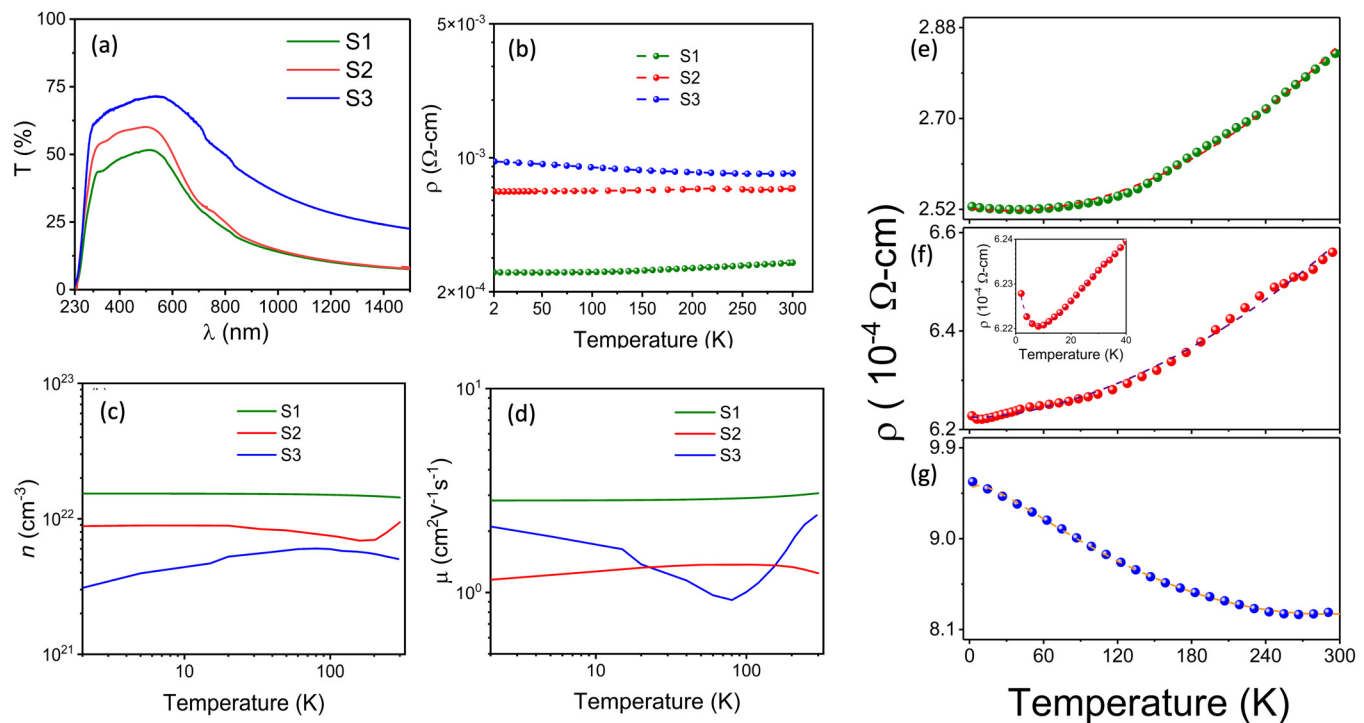
**TABLE I.** Deconvoluted XPS spectra of Nb-3d, showing the contributions of different charge and spin states.

Sample	Charge state	+5/2			+3/2			$\text{Nb}^{4+}/(\text{Nb}^{4+} + \text{Nb}^{5+})$
		Peak positions (eV)	FWHM	Area %	Peak positions (eV)	FWHM	Area %	
S1	+5	207	1.2	53.3	209.7	1.2	36.2	10.5%
	+4	205.9	1.5	6.3	208.5	1.5	4.2	
S2	+5	207	1.2	58.4	209.7	1.2	38.7	2.9%
	+4	205.9	1.5	1.7	208.5	1.5	1.2	

$\sim 10^{-6}$  to  $\sim 10^{-5}$  mbar, which is closer to  $p\text{O}_2$  used in the present study. The role of O on the shift in  $\omega_p$  is confirmed independently by Khan *et al.*,<sup>24</sup> where a change in the composition from  $\text{SrNbO}_3$  to  $\text{Sr}_5\text{Nb}_5\text{O}_{17}$  decreases the absorbance in the visible region and thus increases the transparency.

The electrical and Hall transport measurements are performed using a PPMS with the standard van der Pauw geometry. Figure 4(b) represents the resistivity as a function of the temperature. The resistivity of the samples increases from  $\sim 2.8$  to  $8.1 \times 10^{-4} \Omega \text{ cm}$  at the room temperature as  $p\text{O}_2$  is varied from  $10^{-6}$  to  $5 \times 10^{-5}$  mbar. This is expected since the resistivity depends on the free carriers in the system and as seen from XPS, the contribution of  $\text{Nb}^{4+}$  decreases as

the growth  $p\text{O}_2$  increases. This decreases the amount of free carriers in the system as which is shown in Fig. 4(c) represents the carrier concentration. As evident from Fig. 4(c), the free electron density for S1 reaches  $\sim 10^{22} \text{ cm}^{-3}$  at room temperature and it decreases to  $9 \times 10^{21} \text{ cm}^{-3}$  in the case of S2 and  $5 \times 10^{21} \text{ cm}^{-3}$  for S3. The mobility of the samples shown in Fig. 4(d) on the other hand does not vary much among the samples and is highest for sample S1 at  $3.2 \text{ cm}^2 \text{ V}^{-1} \text{ s}^{-1}$ . On the other hand, for S2 and S3, the mobility is found to be  $\sim 1.2$  and  $2.1 \text{ cm}^2 \text{ V}^{-1} \text{ s}^{-1}$  at the room temperature [Fig. 4(d)]. This reveals that the resistivity, and thus the charge carrier concentration and their mobility also depend slightly on the growth pressure. The mobilities and carrier concentration obtained here



06 January 2024 07:46:46

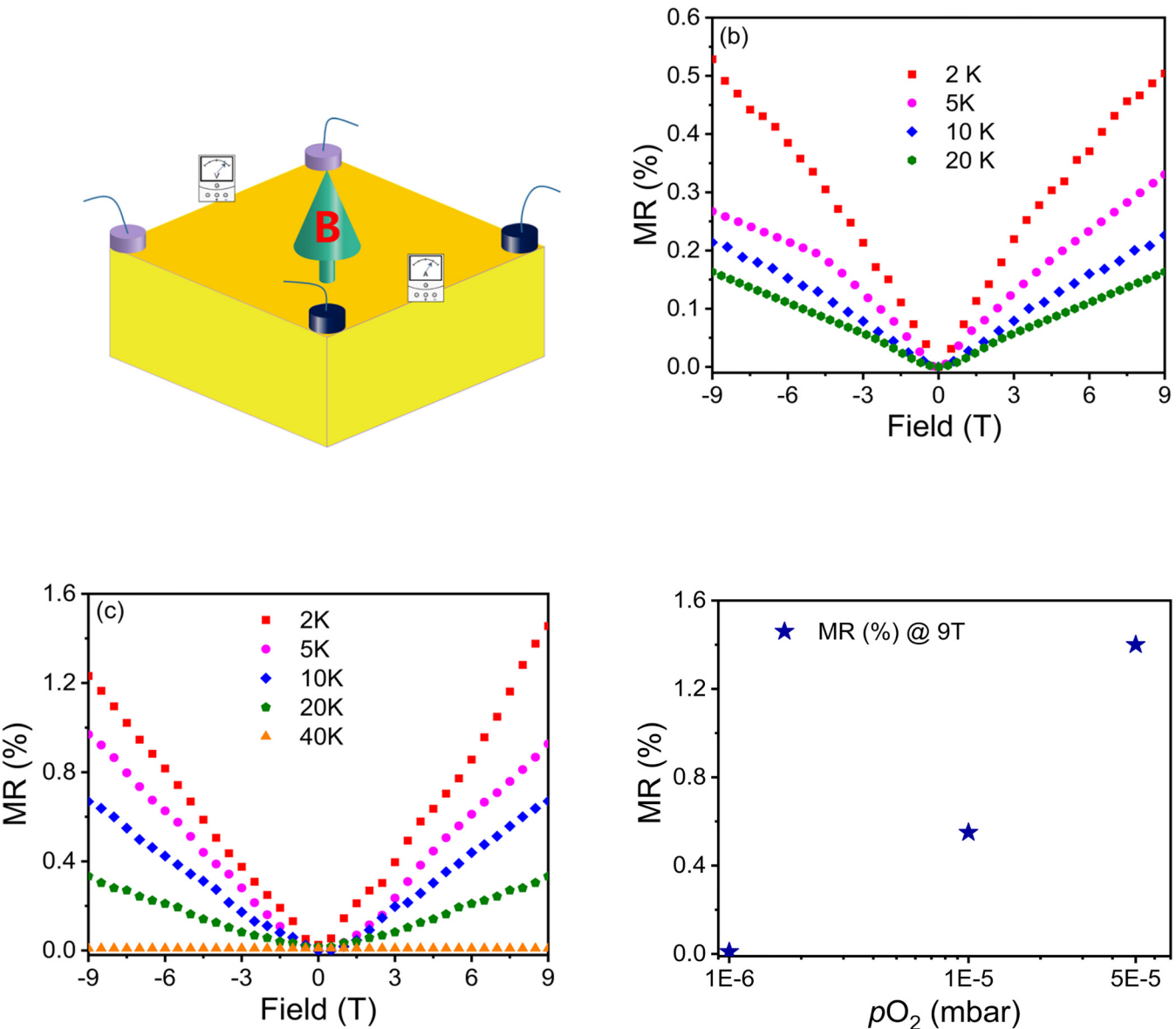
**FIG. 4.** (a) Optical transmittance spectra of all the samples showing an increase in the transparency as the growth  $p\text{O}_2$  is increased. (b) Resistivity–temperature graph for SNO samples grown at different oxygen partial pressures. (c) Carrier concentration and (d) mobility using Hall measurements for all the samples. (e) The resistivity curve for sample S1 is fitted using Eq. (2) whereas (f) S2 and (g) is fitted using Eq. (1). Inset of (f) shows the resistivity curve at low temperatures and transition from metal-like to semiconductor-like feature for sample S2.

**TABLE II.** The parameters  $a_1$ ,  $a_2$ , and  $B$  extracted by fitting samples S1, S2, and S3 using the respective fitting equations mentioned above.

Sample	$\sigma_0$ ( $\text{S cm}^{-1}$ )	$a_1$	$a_2$	$B$	QCC
S1	3968.25	...	...	$4.51 \times 10^{-10}$	No
S2	1600.85	1.83	4.84	$1.93 \times 10^{-10}$	Yes
S3	1060.01	3.19	8.15	$1.22 \times 10^{-9}$	Yes

match the previously obtained<sup>12,16</sup> results for PLD grown SNO thin films deposited on LAO,  $(\text{LaAlO}_3)_{0.3}\text{-(Sr}_2\text{AlTaO}_6)_{0.7}$  (LSAT), and  $\text{GdScO}_3$  (GSO) substrates, where the mobility varies from 0.1 to  $5 \text{ cm}^2 \text{ V}^{-1} \text{ s}^{-1}$  as a function of growth  $p\text{O}_2$ .

It is seen from Figs. 4(e) 4(f), and 4(g) all these resistivity-temperature ( $\rho$ - $T$ ) curves exhibit different nature at low temperatures. The  $\rho$ - $T$  graph for S1 [Fig. 4(e)] shows direct-relationship with temperature ( $\delta\rho/\delta T > 0$ ), decreasing as the temperature



06 January 2024 07:46:46

**FIG. 5.** (a) Schematic of the magnetotransport measurement configuration. MR of sample (b) S2 (c) S3, and (d) Maximum MR for all samples under the same field grown at different oxygen partial pressures.

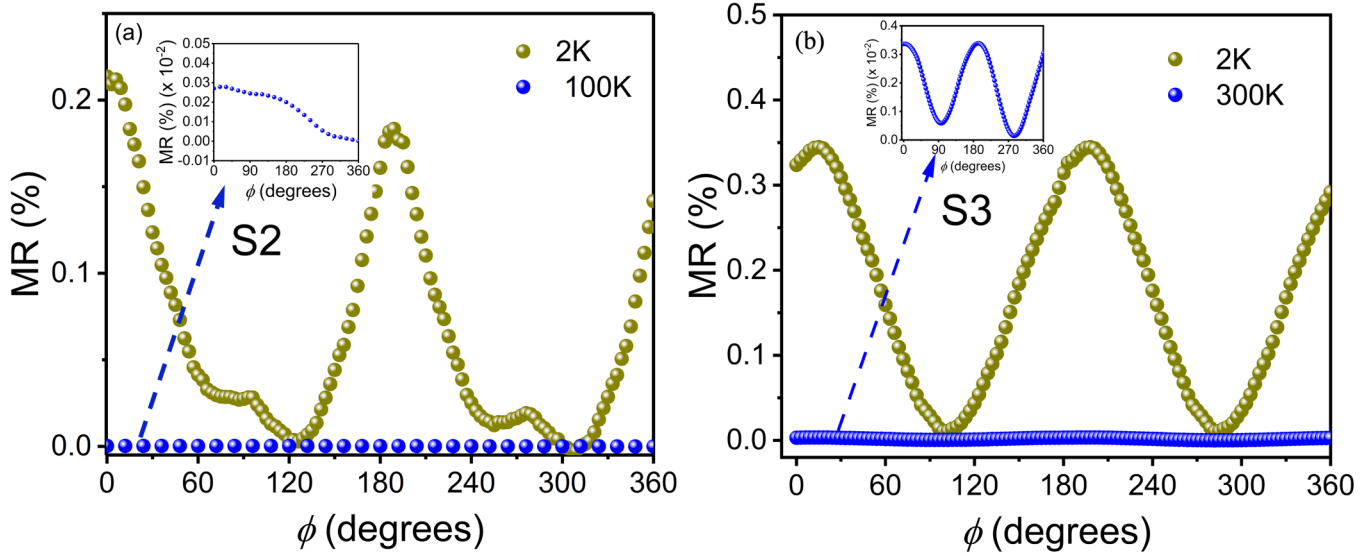


**FIG. 6.** Anisotropic MR study of the samples (a) S2 and (b) S3. The x axis represents the angle between the applied current and the magnetic field. The inset in (a) shows that AMR vanishes completely at 100 K for sample S2 while (b) shows AMR at 300 K, which retains the same twofold symmetry albeit with a much lower value.

decreases justifying its metallic character. However, in sample S2 [Fig. 4(f)], two features are noted. Initially,  $\rho$  is shown to have the same metallic character as S1, however, an upturn in resistivity curve is observed at  $\sim 10$  K, changing its metallic-like features to a semiconducting-like character ( $\delta\rho/\delta T < 0$ ) [see the inset of Fig. 4(f)]. In contrast, sample S3 [Fig. 4(g)] exhibits purely semiconductor-like behavior throughout the whole temperature range. A comparative zoomed-in curve of S1 and S2 is shown in Fig. SI-5 in the [supplementary material](#), to show the different behavior of the resistivity curve for the two samples at low temperatures. The upturn in the resistivity curves is explained by the quantum correction to the conductivity (QCC). For sample S2 and S3, the data given in Figs. 4(f) and 4(g) are fitted using the QCC in the 3D limit, given by<sup>28,29,44</sup>

$$\rho(T) = \frac{1}{\sigma_0 + a_1 T^{p/2} + a_2 T^{1/2}} + BT^2. \quad (1)$$

Here,  $\sigma_0$  is the residual conductivity which is present due to the presence of imperfections in the crystal. The term  $a_1 T^{p/2}$  represents the contribution from the WL term, where  $p=2$  for electron-electron interaction and  $p=3$  for electron-phonon interaction. The term  $a_2 T^{1/2}$  represents the contribution from the REEI and  $BT^2$  term is the Boltzmann term that accounts for the classical low-temperature behavior of the resistivity and Matthiessen rule to hold.<sup>44</sup>

WL arises from the self-interference of the wave packets as they are backscattered by the impurities or other defects. This self-interference leads to an enhancement of the resistivity. REEI occurs due to the renormalization of the effective electron-electron interactions and resulting modifications of the density of states at Fermi

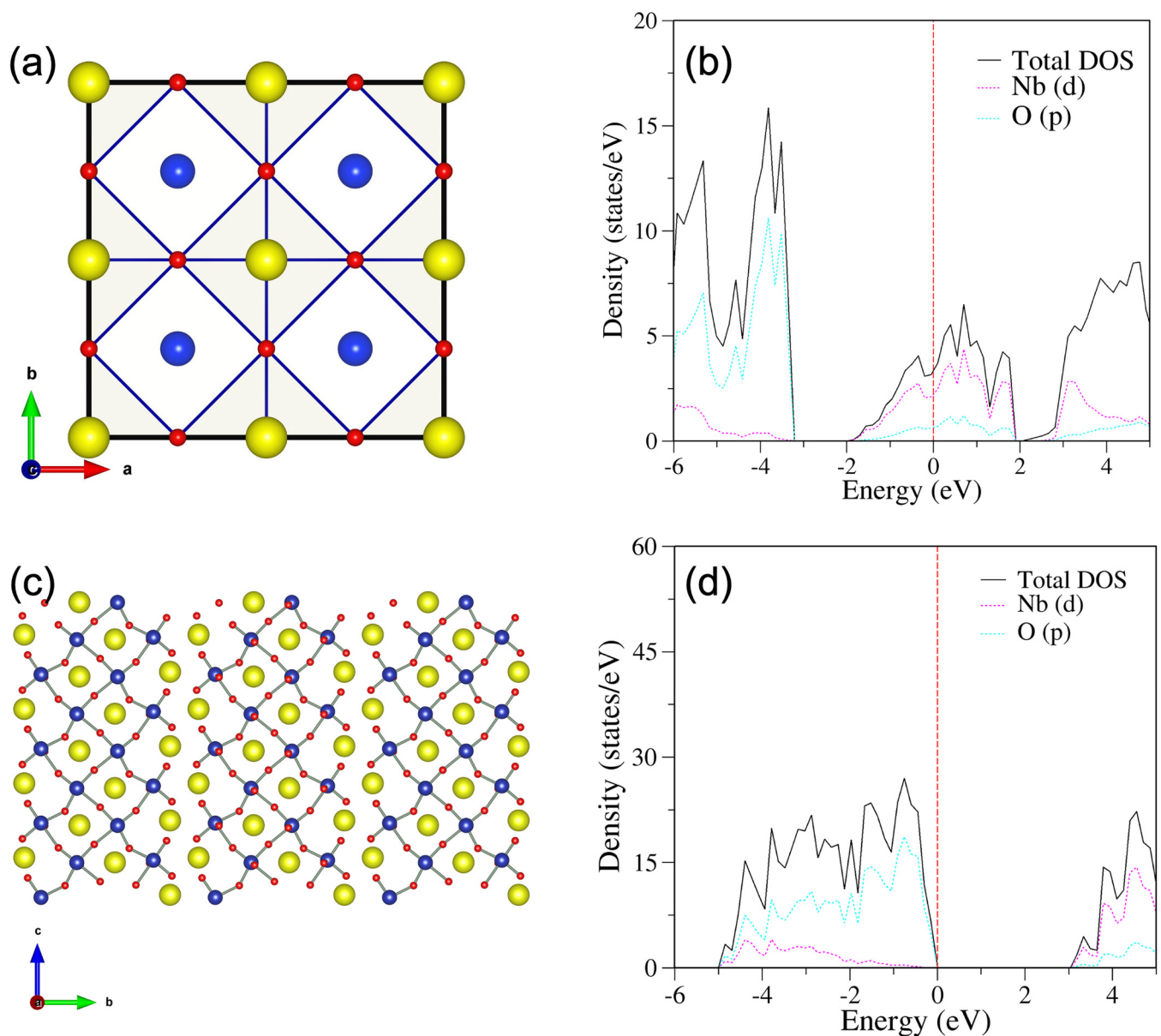
energy.<sup>44,45</sup> By applying a magnetic field, the WL term can be suppressed, since the field destroys the wave coherence, and thus, the self-interference, as a result of which negative magnetoresistance can be obtained.<sup>44,45</sup> In the case of REEI, the field splits the spin of the electrons and due to orbital effects the resistance of the sample increases with an increase in the magnetic field.<sup>44,45</sup> It must also be mentioned here that when there is no contribution from WL and REEI (i.e.,  $a_1 = a_2 = 0$ ), the equation simply is the Boltzmann conductivity formula

$$\rho(T) = \rho_0 + BT^2. \quad (2)$$

For sample S1, the fitting is done by Eq. (2) [dashed lines, Fig. 4(e)]. The fitting for sample S2 and S3 shown in Figs. 4(f) and 4(g) is performed by Eq. (1) (dashed lines). The fitted parameters obtained from all these fittings are given in Table II.

It is seen from Table II that  $a_2 > a_1$  which implies that REEI is the dominant part within the QCC and is responsible for the upturn of resistivity in samples S2 and S3, whereas sample S1 shows no QCC effect. To further verify the dominance of REEI or WL on the QCC, MR measurement is performed on sample S2 and S3 to establish the dominance between WL and REEI in the sample. Figure 5(a) represents the schematic for the MR measurement. A magnetic field is applied in the perpendicular direction to the current in the sample and resistance is measured. Figures 5(b) and 5(c) represent the measured magnetoresistance of the samples S2 and S3. As evident from Figs. 5(b) and 5(c), the MR is positive in all the cases, indicating that REEI is responsible for the upturn in resistivity. The MR decreases as the temperature is increased for both the samples. In the former case, the MR vanishes after 20 K while in the latter case it vanishes at around 40 K. The maximum





06 January 2024 07:46:46

**FIG. 7.** (a) Structure of perovskite  $\text{SrNbO}_3$ , where Sr is denoted by yellow, Nb by blue, and oxygen by red. (b) Density and partial density of states (DOS and PDOS) for the perovskite  $\text{SrNbO}_3$ . (c) Structure of  $\text{SrNbO}_{3.5}$  and (d) density and partial density of states (DOS and PDOS) for  $\text{SrNbO}_{3.5}$ .

values of MR at 2 K and 9 T as a function of growth pressure is given in Fig. 5(d), indicating that MR can only be observed at intermediate growth pressures (intermediate resistivity) and not in very high ( $10^{-4}$  mbar; insulator-like) or very low ( $10^{-6}$  mbar; metallic-like) growth  $p\text{O}_2$ . This type of behavior is seen previously in the case of  $\text{LaNiO}_3$  of varying thickness, where very thin (insulator-like) and very thick (metallic-like) samples does not show any MR, whereas samples with intermediate thickness (intermediate

resistivity) exhibit MR which arises due to variable range hopping mechanism (VRH).<sup>27</sup> Similarly,  $\text{SrVO}_3$ <sup>32</sup> and  $\text{SrMoO}_3$ <sup>28</sup> exhibit a MR of 0.14% and 0.4% for the intermediate resistivity range due to either REEI or VRH.

In addition, as a result of the residual strain in the SNO films, S2 and S3 exhibit an anisotropic behavior during magnetoresistance measurement.<sup>46,47</sup> This anisotropic MR is obtained with respect to the angle ( $\phi$ ) between the applied current and the

magnetic field which varies from 0 to 360°. Figures 6(a) and 6(b) show the angle-dependent magnetoresistance (*AdMR*) of samples S2 and S3.

*AdMR* is calculated using the following expression:<sup>48,49</sup>

$$A = \frac{\rho(0) - \rho(\phi)}{\rho(\phi)} \times 100 \%, \quad (3)$$

where  $\rho(0)$  and  $\rho(\phi)$  signify the resistivities at the respective angles. A twofold symmetric signal is observed here, which can be attributed to the tetragonal magneto-crystalline anisotropy<sup>46,50</sup> for both the samples. It arises due to the strain in the films which are elongated along the *c*-direction. The compressive strain introduces an easy and a hard axis in the system. As seen from Figs. 6(a) and 6(b), the easy axis is along the perpendicular direction (*c* axis) since the resistance is lowest at this point and highest along the in-plane axis (*a* axis), indicating that hard axis is present along the in-plane direction. The AMR for sample S2 [Fig. 6(a)] decreases dramatically as soon as the temperature increases to 100 K but decreases gradually for sample S3 [Fig. 6(b)], and retains its nature even at room temperature.

## D. Theoretical results

To robustly support the experimental results and demonstrate to role of oxygen content on the electronic properties, density functional theory-based simulations are performed on two different stoichiometries of SNO to replicate different environments of growth: (i) SrNbO<sub>3</sub> (Pm3m space group) and (ii) SrNbO<sub>3.5</sub> (Cmc2<sub>1</sub> space group). The optimized structure and density of states (DOS) illustrating electronic properties of SrNbO<sub>3</sub> and SrNbO<sub>3.5</sub> are depicted in Fig. 7.

SrNbO<sub>3</sub> is found to crystallize in cubic structures with  $a = b = c = 4.12 \text{ \AA}$  and  $\alpha = \beta = \gamma = 90^\circ$  [Fig. 7(a)] and a well-organized atomic arrangement of Sr, Nb, and O atoms in a perovskite-type structure, while SrNbO<sub>3.5</sub> crystallizes in a orthorhombic phase with  $a = 4.05 \text{ \AA}$ ,  $b = 27.72 \text{ \AA}$ ,  $c = 5.78 \text{ \AA}$  and  $\alpha = \beta = \gamma = 90^\circ$  [Fig. 7(c)] and a distorted arrangement of compositional atoms. On comparing the electronic properties of both the compounds, it is found that SrNbO<sub>3.5</sub> is an incipient insulator [Fig. 7(d)], whereas SrNbO<sub>3</sub> [Fig. 7(b)] is a metallic system. This transition from an insulator to metallic phase can be understood by Bader charge analysis of the central atom, i.e., Nb. The Bader charge analysis on the Nb ion in each structure provides the information for the free electron in the system. In the case of SNO<sub>3.5</sub>, the charge on Nb is found to be 4.41  $\bar{e}$  whereas for SrNbO<sub>3</sub> it is calculated as 3.53  $\bar{e}$  (see Table ST1 in the [supplementary material](#) for full details), indicating the Nb<sup>5+</sup> state in the former case as compared to Nb<sup>4+</sup> state for the latter. This is consistent with the chemical and electronic data observed in XPS and PPMS measurements, which reveal that the metallic character of samples can be explained by the large number of Nb<sup>4+</sup> present in the sample. As the contribution of Nb<sup>4+</sup> is decreased (and subsequently Nb<sup>5+</sup> contribution increases), an increase in the resistivity is seen. Overall, both measurements and first-principles simulations elucidate that the insulator-metal transition in SNO is dictated by the influence of O in the system.

## IV. CONCLUSION

In conclusion, the influence of O partial pressure in the range of  $1 \times 10^{-6}$ – $5 \times 10^{-5}$  mbar during the growth process on the structural, chemical, optical, electronic, and magnetoresistive properties of PLD deposited epitaxial (001) SNO thin films on (001) LAO is studied. In each case, single phases having tetragonal structures are observed, arising due to the residual compressive strain imparted by the substrate. AFM and FESEM data show the uniform distribution of Sr, Nb, and O over the entire surface without any grains or phase boundaries. The stoichiometry of the film throughout the samples confirmed by EDX and RBS is SrNbO<sub>3±δ</sub>. The room temperature resistivity increases from  $2.8 \times 10^{-4}$  to  $8.1 \times 10^{-4} \Omega\text{-cm}$  as the  $pO_2$  increases. An upturn is seen in the resistivity curves above  $1 \times 10^{-6}$  mbar  $pO_2$  or films grown under  $pO_2$  of  $1 \times 10^{-5}$  and  $5 \times 10^{-5}$  mbar, which signifies some electronic disorder in the system. This is consistent with the result of HR-XPS analysis, in which the Nb<sup>5+</sup> charge state is observed throughout the high resistive film, while a significant contribution from Nb<sup>4+</sup> is seen in the low-resistive film. This change of the Nb charge state is also supported by the present theoretical calculation, in which the O-content is varied and its influence on the electronic conductivity is studied. The cause for the upturn in the resistivity is attributed to the REEI part of QCC. The REEI is further confirmed by the MR measurement and the highest value of +1.5% is achieved in sample grown under  $pO_2$  of  $5 \times 10^{-5}$  mbar. Moreover, AMR of 0.35% is also observed in this film. All the above studies identify that SNO is a highly versatile tunable material, in which the optoelectronic and magnetic properties can be varied just by the manipulation of O during the growth process. The manipulation of SNO during growth further paves the way to explore and design its potential in the next-generation of optoelectronic based devices.

## SUPPLEMENTARY MATERIAL

See the supplementary material for VASE, AFM, FESEM, RBS, optical bandgap, and the zoomed-in resistivities of S1 and S2 to shed light on their behavior at low temperatures. The file also contains the complete description of composition and thickness obtained by RBS and Bader charges of all atoms computed from DFT in a tabular form.

## ACKNOWLEDGMENTS

We acknowledge support of the research funding from Shiv Nadar Institution of Eminence (Deemed to be University) (Grant No. SNS/PHY/2013-20) and DST-Science and Engineering Research Board (SERB) India (Grant No. SR/FST/PS-I/2017/6C). For theoretical calculation, the high-performance computing facility provided by the School of Natural Sciences, Shiv Nadar Institution of Eminence (Deemed to be University) is utilized. We would also like to thank A. Mitra, V. Kumar, S. Ghosh, H. Arora, S. P. Singh, U. Mukherjee, D. Chakraborty, and R. Sen for their support and invaluable discussions.

## AUTHOR DECLARATIONS

### Conflict of Interest

The authors have no conflicts to disclose.

## Author Contributions

**Shammi Kumar:** Conceptualization (equal); Data curation (equal); Formal analysis (equal); Investigation (equal); Methodology (equal); Software (equal); Validation (equal); Visualization (equal); Writing – original draft (lead); Writing – review & editing (equal). **Jibril Ahammad:** Formal analysis (equal); Software (equal); Writing – review & editing (equal). **Dip Das:** Formal analysis (equal); Software (equal); Writing – review & editing (equal). **Rakesh Kumar:** Data curation (equal); Methodology (equal). **Sankar Dhar:** Conceptualization (equal); Formal analysis (equal); Resources (equal); Supervision (equal); Writing – review & editing (equal). **Priya Johari:** Conceptualization (equal); Formal analysis (equal); Funding acquisition (equal); Project administration (equal); Supervision (equal); Writing – review & editing (equal).

## DATA AVAILABILITY

The data that support the findings of this study are available from the corresponding author upon reasonable request.

## REFERENCES

- <sup>1</sup>X. Xu, C. Randorn, P. Efstathiou, and J. T. S. Irvine, “A red metallic oxide photocatalyst,” *Nat. Mater.* **11**(7), 595–598 (2012).
- <sup>2</sup>J. Bruncko, P. Šutta, M. Netrvalová, M. Michalka, and A. Vincze, “Pulsed laser deposition of Ga doped ZnO films—Influence of deposition temperature and laser pulse frequency on structural, optical and electrical properties,” *Vacuum* **159**, 134–140 (2019).
- <sup>3</sup>J. Roth, A. Paul, N. Goldner, A. Pogrebnjakov, K. Agueda, T. Birol, N. Alem, and R. Engel-Herbert, “Sputtered  $\text{Sr}_x\text{NbO}_3$  as a UV-transparent conducting film,” *ACS Appl. Mater. Interfaces* **12**(27), 30520–30529 (2020).
- <sup>4</sup>S. Kumar, “Exploration of structural, morphological and magnetic properties of transition metal doped  $\text{SnO}_2$  films grown using pulsed laser deposition,” *Vacuum* **182**, 109725 (2020).
- <sup>5</sup>J. Bruncko, P. Šutta, M. Netrvalová, M. Michalka, A. Vincze, and J. Kovac, “Comparative study of ZnO thin film prepared by pulsed laser deposition—Comparison of influence of different ablative lasers,” *Vacuum* **138**, 184–190 (2017).
- <sup>6</sup>C. Rodenbücher, G. Bihlmayer, C. Korte, and K. Szot, “Gliding of conducting dislocations in  $\text{SrTiO}_3$  at room temperature: Why oxygen vacancies are strongly bound to the cores of dislocations,” *APL Mater.* **11**(2), 021108 (2023).
- <sup>7</sup>Y. Iwasaki, Y. Mizuno, T. Nakayama, and T. Suzuki, “Preparation of Cr–Si–N–O thin films epitaxially grown on MgO substrates by pulsed laser deposition,” *Vacuum* **179**, 109498 (2020).
- <sup>8</sup>J. Zhang, J. M. Ok, Y.-Y. Pai, J. Lapano, E. Skoropata, A. R. Mazza, H. Li, A. Huon, S. Yoon, B. Lawrie, M. Brahlek, T. Z. Ward, G. Eres, H. Miao, and H. N. Lee, “Extremely large magnetoresistance in high-mobility  $\text{SrNbO}_3/\text{SrTiO}_3$  heterostructures,” *Phys. Rev. B* **104**(16), L161404 (2021).
- <sup>9</sup>J. M. Ok, N. Mohanta, J. Zhang, S. Yoon, S. Okamoto, E. S. Choi, H. Zhou, M. Briggeman, P. Irvin, A. R. Lupini, Y.-Y. Pai, E. Skoropata, C. Sohn, H. Li, H. Miao, B. Lawrie, W. S. Choi, G. Eres, J. Levy, and H. N. Lee, “Correlated oxide Dirac semimetal in the extreme quantum limit,” *Sci. Adv.* **7**(38), eabf9631 (2021).
- <sup>10</sup>T. Yao, Y. Jiang, C. Chen, X. Yan, A. Tao, L. Yang, C. Li, K. Sugo, H. Ohta, H. Ye, Y. Ikuhara, and X. Ma, “Ferroelectric oxide thin film with an out-of-plane electrical conductivity,” *Nano Lett.* **20**(2), 1047–1053 (2020).
- <sup>11</sup>D. Wan, B. Yan, J. Chen, S. Wu, J. Hong, D. Song, X. Zhao, X. Chi, S. Zeng, Z. Huang, C. Li, K. Han, W. Zhou, Y. Cao, A. Rusydi, S. J. Pennycook, P. Yang, Ariando, R. Xu, Q.-H. Xu, X. R. Wang, and T. Venkatesan, “New family of plasmonic photocatalysts without noble metals,” *Chem. Mater.* **31**(7), 2320–2327 (2019).
- <sup>12</sup>M. Mirjole, M. Kataja, T. K. Hakala, P. Komissinskiy, L. Alff, G. Herranz, and J. Fontcuberta, “Optical plasmon excitation in transparent conducting  $\text{SrNbO}_3$  and  $\text{SrVO}_3$  thin films,” *Adv. Optical Mater.* **9**, 2100520 (2021).
- <sup>13</sup>M. B. Cortie, M. D. Arnold, and V. J. Keast, “The quest for zero loss: Unconventional materials for plasmonics,” *Adv. Mater.* **32**(18), 1904532 (2020).
- <sup>14</sup>A. Paul and T. Birol, “Strain tuning of plasma frequency in vanadate, niobate, and molybdate perovskite oxides,” *Phys. Rev. Mater.* **3**(8), 085001 (2019).
- <sup>15</sup>D. Song, D. Wan, H.-H. Wu, D. Xue, S. Ning, M. Wu, T. Venkatesan, and S. J. Pennycook, “Electronic and plasmonic phenomena at nonstoichiometric grain boundaries in metallic  $\text{SrNbO}_3$ ,” *Nanoscale* **12**(12), 6844–6851 (2020).
- <sup>16</sup>D. Y. Wan, Y. L. Zhao, Y. Cai, T. C. Asmara, Z. Huang, J. Q. Chen, J. Hong, S. M. Yin, C. T. Nelson, M. R. Motapothula, B. X. Yan, D. Xiang, X. Chi, H. Zheng, W. Chen, R. Xu, Ariando, A. Rusydi, A. M. Minor, M. B. H. Breese, M. Sherburne, M. Asta, Q.-H. Xu, and T. Venkatesan, “Electron transport and visible light absorption in a plasmonic photocatalyst based on strontium niobate,” *Nat. Commun.* **8**(1), 15070 (2017).
- <sup>17</sup>L. Si, J. Kaufmann, Z. Zhong, J. M. Tomczak, and K. Held, “Pitfalls and solutions for perovskite transparent conductors,” *Phys. Rev. B* **104**(4), L041112 (2021).
- <sup>18</sup>T. C. Asmara, F. Lichtenberg, F. Biebl, T. Zhu, P. K. Das, M. A. Naradipa, A. D. Fauzi, C. Diao, P. Yang, P. Lenzen, S. Buchenau, B. Grimm-Lebsanft, D. Wan, P. E. Trevisanutto, M. B. H. Breese, T. Venkatesan, M. Rübhausen, and A. Rusydi, “Photoinduced metastable dd-exciton-driven metal-insulator transitions in quasi-one-dimensional transition metal oxides,” *Commun. Phys.* **3**(1), 206 (2020).
- <sup>19</sup>C. Bhattacharya, S. E. Saji, A. Mohan, V. Madav, G. Jia, and Z. Yin, “Sustainable nanoplasmon-enhanced photoredox reactions: Synthesis, characterization, and applications,” *Adv. Energy Mater.* **10**(40), 2002402 (2020).
- <sup>20</sup>D. Oka, Y. Hirose, S. Nakao, T. Fukumura, and T. Hasegawa, “Intrinsic high electrical conductivity of stoichiometric  $\text{SrNbO}_3$  epitaxial thin films,” *Phys. Rev. B* **92**(20), 205102 (2015).
- <sup>21</sup>C. Bigi, P. Orgiani, J. Ślawińska, J. Fujii, J. T. Irvine, S. Picozzi, G. Panaccione, I. Vobornik, G. Rossi, D. Payne, and F. Borgatti, “Direct insight into the band structure of  $\text{SrNbO}_3$ ,” *Phys. Rev. Mater.* **4**(2), 025006 (2020).
- <sup>22</sup>C. Chen, D. Yin, K. Inoue, F. Lichtenberg, X. Ma, Y. Ikuhara, and J. G. Bednorz, “Atomic-scale origin of the quasi-one-dimensional metallic conductivity in strontium niobates with perovskite-related layered structures,” *ACS Nano* **11**(12), 12519–12525 (2017).
- <sup>23</sup>M. Mohammadi, R. Xie, N. Hadaeghi, A. Radetina, A. Arzumano, P. Komissinskiy, H. Zhang, and L. Alff, “Tailoring optical properties in transparent highly conducting perovskites by cationic substitution,” *Adv. Mater.* **35**(7), 2206605 (2023).
- <sup>24</sup>M. R. Khan, H. R. Gopidi, and O. I. Malyi, “Optical properties and electronic structures of intrinsic gapped metals: Inverse materials design principles for transparent conductors,” *Appl. Phys. Lett.* **123**(6), 061101 (2023).
- <sup>25</sup>T. C. Asmara, D. Wan, Y. Zhao, M. A. Majidi, C. T. Nelson, M. C. Scott, Y. Cai, B. Yan, D. Schmidt, M. Yang, T. Zhu, P. E. Trevisanutto, M. R. Motapothula, Y. P. Feng, M. B. H. Breese, M. Sherburne, M. Asta, A. Minor, T. Venkatesan, and A. Rusydi, “Tunable and low-loss correlated plasmons in Mott-like insulating oxides,” *Nat. Commun.* **8**(1), 15271 (2017).
- <sup>26</sup>P. Di Pietro, C. Bigi, S. K. Chaluvadi, D. Knez, P. Rajak, R. Ciancio, J. Fujii, F. Mercuri, S. Lupi, G. Rossi, F. Borgatti, A. Perucchi, and P. Orgiani, “Oxygen-driven metal-insulator transition in  $\text{SrNbO}_3$  thin films probed by infrared spectroscopy,” *Adv. Electr. Mater.* **8**(7), 2101338 (2022).
- <sup>27</sup>R. Scherwitzl, S. Gariglio, M. Gabay, P. Zubko, M. Gibert, and J.-M. Triscone, “Metal-Insulator transition in ultrathin  $\text{LaNiO}_3$  films,” *Phys. Rev. Lett.* **106**(24), 246403 (2011).
- <sup>28</sup>M. Zhu, P. Li, L. Hu, R. Wei, J. Yang, W. Song, X. Zhu, and Y. Sun, “Thickness dependence of metal-insulator transition in  $\text{SrMoO}_3$  thin films,” *J. Appl. Phys.* **132**(7), 075303 (2022).
- <sup>29</sup>M. Nistor, F. Gherendi, N. B. Mandache, C. Hebert, J. Perrière, and W. Seiler, “Metal-semiconductor transition in epitaxial ZnO thin films,” *J. Appl. Phys.* **106**(10), 103710 (2009).

- <sup>30</sup>X. D. Liu, E. Y. Jiang, and Z. Q. Li, "Low temperature electrical transport properties of B-doped ZnO films," *J. Appl. Phys.* **102**(7), 073708 (2007).
- <sup>31</sup>A. Molinari, F. Balduini, L. Rocchino, R. Wawrzyńczak, M. Sousa, H. Bui, C. Lavoie, V. Stanic, J. Jordan-Sweet, M. Hopstaken, S. Tchoumakov, S. Franca, J. Gooth, S. Fratini, A. G. Grushin, C. Zota, B. Gotsmann, and H. Schmid, "Disorder-Induced magnetotransport anomalies in amorphous and textured  $\text{Co}_{1-x}\text{Si}_x$  semimetal thin films," *ACS Appl. Electron. Mater.* **5**(5), 2624–2637 (2023).
- <sup>32</sup>C. Wang, H. Zhang, K. Deepak, C. Chen, A. Fouchet, J. Duan, D. Hilliard, U. Kentsch, D. Chen, M. Zeng, X. Gao, Y.-J. Zeng, M. Helm, W. Prellier, and S. Zhou, "Tuning the metal-insulator transition in epitaxial  $\text{SrVO}_3$  films by uniaxial strain," *Phys. Rev. Mater.* **3**(11), 115001 (2019).
- <sup>33</sup>G. Kresse and D. Joubert, "From ultrasoft pseudopotentials to the projector augmented-wave method," *Phys. Rev. B* **59**(3), 1758–1775 (1999).
- <sup>34</sup>P. E. Blöchl, "Projector augmented-wave method," *Phys. Rev. B* **50**(24), 17953–17979 (1994).
- <sup>35</sup>J. P. Perdew, K. Burke, and M. Ernzerhof, "Generalized gradient approximation made simple," *Phys. Rev. Lett.* **77**(18), 3865–3868 (1996).
- <sup>36</sup>S. L. Dudarev, G. A. Botton, S. Y. Savrasov, C. J. Humphreys, and A. P. Sutton, "Electron-energy-loss spectra and the structural stability of nickel oxide: An LSDA + U study," *Phys. Rev. B* **57**(3), 1505–1509 (1998).
- <sup>37</sup>S. K. Chaluvadi, D. Mondal, C. Bigi, D. Knez, P. Rajak, R. Ciancio, J. Fujii, G. Panaccione, I. Vobornik, G. Rossi, and P. Orgiani, "Pulsed laser deposition of oxide and metallic thin films by means of Nd:YAG laser source operating at its 1st harmonics: Recent approaches and advances," *J. Phys. Mater.* **4**(3), 032001 (2021).
- <sup>38</sup>P. Orgiani, R. Ciancio, A. Galdi, S. Amoroso, and L. Maritato, "Physical properties of  $\text{La}_{0.7}\text{Ba}_{0.3}\text{MnO}_{3-\delta}$  complex oxide thin films grown by pulsed laser deposition technique," *Appl. Phys. Lett.* **96**(3), 032501 (2010).
- <sup>39</sup>G. Greczynski and L. Hultman, "X-ray photoelectron spectroscopy: Towards reliable binding energy referencing," *Prog. Mater. Sci.* **107**, 100591 (2020).
- <sup>40</sup>G. Greczynski, R. T. Haasch, N. Hellgren, E. Lewin, and L. Hultman, "X-ray photoelectron spectroscopy of thin films," *Nat. Rev. Methods Primers* **3**(1), 40 (2023).
- <sup>41</sup>Z. Zhong and P. Hansmann, "Tuning the work function in transition metal oxides and their heterostructures," *Phys. Rev. B* **93**(23), 235116 (2016).
- <sup>42</sup>T. Hadamek, A. B. Posadas, A. Dhamdhere, D. J. Smith, and A. A. Demkov, "Spectral identification scheme for epitaxially grown single-phase niobium dioxide," *J. Appl. Phys.* **119**(9), 095308 (2016).
- <sup>43</sup>S. Thapa, S. R. Provence, P. T. Gemperline, B. E. Matthews, S. R. Spurgeon, S. L. Battles, S. M. Heald, M. A. Kuroda, and R. B. Comes, "Surface stability of  $\text{SrNbO}_3$  grown by hybrid molecular beam epitaxy," *APL Mater.* **10**(9), 091112 (2022).
- <sup>44</sup>G. Herranz, F. Sánchez, J. Fontcuberta, V. Laukhin, J. Galibert, M. V. García-Cuenca, C. Ferrater, and M. Varela, "Magnetic field effect on quantum corrections to the low-temperature conductivity in metallic perovskite oxides," *Phys. Rev. B* **72**(1), 014457 (2005).
- <sup>45</sup>P. A. Lee and T. V. Ramakrishnan, "Disordered electronic systems," *Rev. Mod. Phys.* **57**(2), 287–337 (1985).
- <sup>46</sup>T. Li, L. Zhang, and X. Hong, "Anisotropic magnetoresistance and planar Hall effect in correlated and topological materials," *J. Vac. Sci. Technol. A* **40**(1), 010807 (2022).
- <sup>47</sup>R. Niu and W. K. Zhu, "Materials and possible mechanisms of extremely large magnetoresistance: A review," *J. Phys.: Condens. Matter* **34**(11), 113001 (2022).
- <sup>48</sup>M. Vagadia, J. Sahoo, A. Kumar, S. Sardar, T. M. Tank, and D. S. Rana, "Rashba spin-orbit coupling induced modulation of magnetic anisotropy in canted antiferromagnetic heterostructures," *Phys. Rev. B* **107**(6), 064420 (2023).
- <sup>49</sup>M. Vagadia, S. Sardar, T. Tank, S. Das, B. Gunn, P. Pandey, R. Hübner, F. Rodolakis, G. Fabbri, Y. Choi, D. Haskel, A. Frano, and D. S. Rana, "Extraordinary anisotropic magnetoresistance in  $\text{CaMnO}_3/\text{CaIrO}_3$  heterostructures," *Phys. Rev. B* **105**(2), L020402 (2022).
- <sup>50</sup>A. A. Burema and T. Banerjee, "Temperature-dependent periodicity halving of the in-plane angular magnetoresistance in  $\text{La}_{0.67}\text{Sr}_{0.33}\text{MnO}_3$  thin films on  $\text{LaAlO}_3$ ," *Appl. Phys. Lett.* **119**(1), 011901 (2021).